Carrier generation and collection in  $\text{Zn}_3\text{P}_2/\text{InP}$  heterojunction solar cells

Rajrupa Paul<sup>a</sup>, Stefan W. Tabernig<sup>c</sup>, Joel Reñé Saper<sup>a</sup>, Julien Hurni<sup>d</sup>, Anja Tiede<sup>a</sup>, Xinyun Liu<sup>e</sup>, Djamshid A. Damry<sup>e</sup>, Vanessa Conti<sup>a</sup>, Mahdi Zamani<sup>a</sup>, Simon Escobar Steinvall<sup>a,1</sup>, Mirjana Dimitrievska<sup>a,f</sup>, Esther Alarcon-Lladó<sup>c</sup>, Valerio Piazza<sup>a</sup>, Jessica Boland<sup>e</sup>, Franz-Josef Haug<sup>d</sup>, Albert Polman<sup>c</sup>, Anna Fontcuberta i Morral<sup>a,b,\*</sup>

<sup>a</sup> Laboratory of Semiconductor Materials, Institute of Materials, School of Engineering, Ecole Polytechnique Fédérale de Lausanne, 1015, Lausanne, Switzerland

<sup>b</sup> Institute of Physics, School of Basic Sciences, Ecole Polytechnique Fédérale de Lausanne, 1015, Lausanne, Switzerland

<sup>c</sup> Center for Nanophotonics, NWO-Institute AMOLF, Science Park 104, 1098 XG, Amsterdam, the Netherlands

<sup>d</sup> Laboratory of Photovoltaics and Thin Film Electronics (PV-Lab), Institute of Electrical and Microengineering, Ecole Polytechnique Fédérale de Lausanne, 2000, Neuchâtel, Switzerland

<sup>e</sup> Photon Science Institute, Department of Electrical and Electronic Engineering, University of Manchester, Alan Turing Building, Oxford Road, Manchester, M13 9PL, UK

<sup>f</sup> Transport at Nanoscale Interfaces Laboratory, Swiss Federal Laboratories for Material Science and Technology (EMPA) Ueberlandstrasse 129, 8600, Duebendorf, Switzerland

## ARTICLE INFO

## Keywords:

$\text{Zn}_3\text{P}_2$  thin films

Earth-abundant semiconductors

Photovoltaics

## ABSTRACT

Zinc phosphide ( $\text{Zn}_3\text{P}_2$ ) has been lauded as a promising solar absorber material due to its functional properties and the abundance of zinc and phosphorous. In the last 4 decades, there has not been any significant improvement in the efficiencies of  $\text{Zn}_3\text{P}_2$ -based solar cells. This is vastly due to the limited understanding of how to tune its optoelectronic properties. Recently, significant progress has been made in the growth and characterization of the material, which has shed light on its potential. In this study, we report an energy conversion efficiency as high as 4.4% for a solar cell based on a polycrystalline  $\text{Zn}_3\text{P}_2/\text{InP}$  heterojunction. This device presents an open circuit voltage of 528.8 mV, 7.5% higher than the  $\text{Zn}_3\text{P}_2$  homojunction record. We investigate the dominant recombination mechanisms within the film using different techniques to identify the key factors underpinning our device efficiency. In particular, we pinpoint that reduced carrier collection at the front of  $\text{Zn}_3\text{P}_2$  is responsible for the reduced collection of high-energy photons. This allows us to suggest the design rules for next-generation  $\text{Zn}_3\text{P}_2$ -based heterojunction solar cells, which should allow us to go beyond the current conversion values.

## 1. Introduction

The need for sustainable electric power generation is strongly pushing the research on novel materials suited for high-performing solar devices [1–4]. Zinc phosphide ( $\text{Zn}_3\text{P}_2$ ) is a highly suitable candidate for the large-scale deployment of photovoltaic technology [5]. It has a direct bandgap at 1.5 eV, which places it close to the optimum bandgap energy value required to reach the Shockley-Queisser limit [6]. In addition, it has been demonstrated that  $\text{Zn}_3\text{P}_2$  exhibits a high absorption coefficient ( $>10^4\text{--}10^5\text{ cm}^{-1}$ ) in the visible range [7,8] and a long minority carrier diffusion length (5–10  $\mu\text{m}$ ), which are both essential criteria for achieving high-efficiency solar cells. Additionally, zinc and

phosphorous are earth-abundant elements with a low cost and high extraction volume. However, despite these promising material characteristics, there has only been incremental improvement in the efficiency values related to  $\text{Zn}_3\text{P}_2$ -based solar cells. The record for highest efficiency was reported in 1981 and has remained for the past few decades at 5.96% for  $\text{Mg}/\text{Zn}_3\text{P}_2$  Schottky junction solar cells [9].

One of the shortcomings of  $\text{Zn}_3\text{P}_2$  is the lack of understanding of how to engineer its carrier density by doping. Zinc vacancies and phosphorous interstitials exhibit relatively low formation energies (which are between 14 meV and 90 meV for phosphorous interstitials and 190 meV–290 meV for zinc vacancies) [10–12], and both act as acceptors in  $\text{Zn}_3\text{P}_2$ . Consequently,  $\text{Zn}_3\text{P}_2$  is naturally p-type. Doping the material

\* Corresponding author. Laboratory of Semiconductor Materials, Institute of Materials, School of Engineering, Ecole Polytechnique Fédérale de Lausanne, 1015, Lausanne, Switzerland.

E-mail address: [anna.fontcuberta-morral@epfl.ch](mailto:anna.fontcuberta-morral@epfl.ch) (A. Fontcuberta i Morral).

<sup>1</sup> Current affiliation: Centre for Analysis and Synthesis and NanoLund, Lund University, Box 124, 221 00 Lund, Sweden.

n-type has proven to be challenging due to the self-compensation effect [13]. This has hindered the fabrication of p-n homojunction solar cells. Instead, the majority of the  $\text{Zn}_3\text{P}_2$ -based solar cells are either heterojunction or Schottky junction solar cells. The Schottky junction solar cells with the highest recorded efficiencies were fabricated on multi-crystalline large grain  $\text{Zn}_3\text{P}_2$  wafers with Mg as the Schottky contact [9]. While similar Schottky junction solar cells fabricated on polycrystalline  $\text{Zn}_3\text{P}_2$  thin films have demonstrated efficiencies close to 4.3% [14]. The reduced efficiency associated with polycrystalline  $\text{Zn}_3\text{P}_2$  thin films is due to the reduced fill factor arising from higher series resistance. Alternatively, heterojunction device architectures have been proposed to overcome the inherent limitations of the Schottky junction solar cells. Some commonly used n-type emitters for  $\text{Zn}_3\text{P}_2$  heterojunction solar cells are ZnO, ZnSe, ZnS, and CdS [15–19]. Even though  $\text{Zn}_3\text{P}_2$  p-n heterojunction solar cells have not shown efficiencies greater than the Schottky junction solar cells, they did demonstrate higher open-circuit voltage and short-circuit current values. For instance, p- $\text{Zn}_3\text{P}_2$ /n-ZnSe solar cells showed an efficiency of 0.8% but demonstrated record high open-circuit voltage of 810 mV [19]. Similarly, an efficiency of 1.1% was obtained with p- $\text{Zn}_3\text{P}_2$ /n-ITO heterojunction solar cell with a short-circuit current value of 18.4 mA/cm<sup>2</sup> [20]. Prior studies on  $\text{Zn}_3\text{P}_2$  heterojunction solar cells indicate the possibility of efficiency enhancement by combining high-quality single-crystalline  $\text{Zn}_3\text{P}_2$  with an optimal heterojunction device design. However, improvement in the crystallinity has so far not translated into enhancement in the efficiency of  $\text{Zn}_3\text{P}_2$ -based solar cells [17,21]. Epitaxial  $\text{Zn}_3\text{P}_2$  thin film grown on a GaAs (001) substrate by Bosco et al. showed a low short-circuit current density (<0.1 mA/cm<sup>2</sup> under 1 Sun simulated illumination) [17]. This hints toward the need for an efficient device architecture capable of harnessing the full potential of  $\text{Zn}_3\text{P}_2$  as a solar absorber material.

In this work, we demonstrate a minimally processed  $\text{Zn}_3\text{P}_2$ -based solar cell, by employing an ITO top contact on a polycrystalline  $\text{Zn}_3\text{P}_2$  thin film, we were able to achieve 4.4% efficiency. We analyze the illumination-dependent electronic behaviour, as well as the external

quantum efficiency to determine the dominant limiting factors of the device. Additionally, we propose a working principle for the device, highlight the role of ITO, and investigate the contribution of  $\text{Zn}_3\text{P}_2$  to the overall working of the device. Finally, we provide an overview of the prospects associated with the next generation of  $\text{Zn}_3\text{P}_2$ -based solar cells.

## 2. Experimental

### 2.1. Materials and device fabrication

Molecular beam epitaxy (MBE) was used for the growth of micron-thick  $\text{Zn}_3\text{P}_2$  films on undoped InP (100) substrates. The growth method is described in detail in Ref. [22]. Under optimal growth conditions, we are able to tune the crystallinity of the  $\text{Zn}_3\text{P}_2$  thin films by controlling the degassing time of the substrate [22]. Short degassing times of 10–20 min result in polycrystalline growth, whereas degassing times of 30–60 min ensure monocrystalline growth. The presence of oxide at the interface determines the crystalline quality of the  $\text{Zn}_3\text{P}_2$  thin film. The schematic representation of the process flow used for fabricating  $\text{Zn}_3\text{P}_2$ -based solar cells is shown in Fig. 1a. A polycrystalline  $\text{Zn}_3\text{P}_2$  thin film was grown on an InP substrate at 265 °C for 240 min. Prior to the device fabrication, the  $\text{Zn}_3\text{P}_2$  surface was cleaned using argon milling in the sputtering chamber for 30–45 s (at an Ar flow of 50 sccm and 100 W power) to remove the native oxide. Subsequently, a transparent conductive oxide (ITO =  $\text{In}_2\text{O}_3$ :SnO = 90%:10%) electrode was sputtered on top. The nominal thickness of the sputtered ITO electrode was ~100 nm, however, depending on the reactor conditions this value could fluctuate by  $\pm 10\%$ . Before the deposition of the top grid, 100 nm of Au was sputtered onto the rear of the InP substrate to act as the back contact. Finally, the top Ag finger grid was deposited by sputtering using a shadow mask. Fig. 1b shows the schematic representation of the fabricated device and Fig. 1c shows the photograph of a completely fabricated device, having a total surface area of ~0.65 cm<sup>2</sup> and an active area available for photon absorption of 0.467 cm<sup>2</sup>.

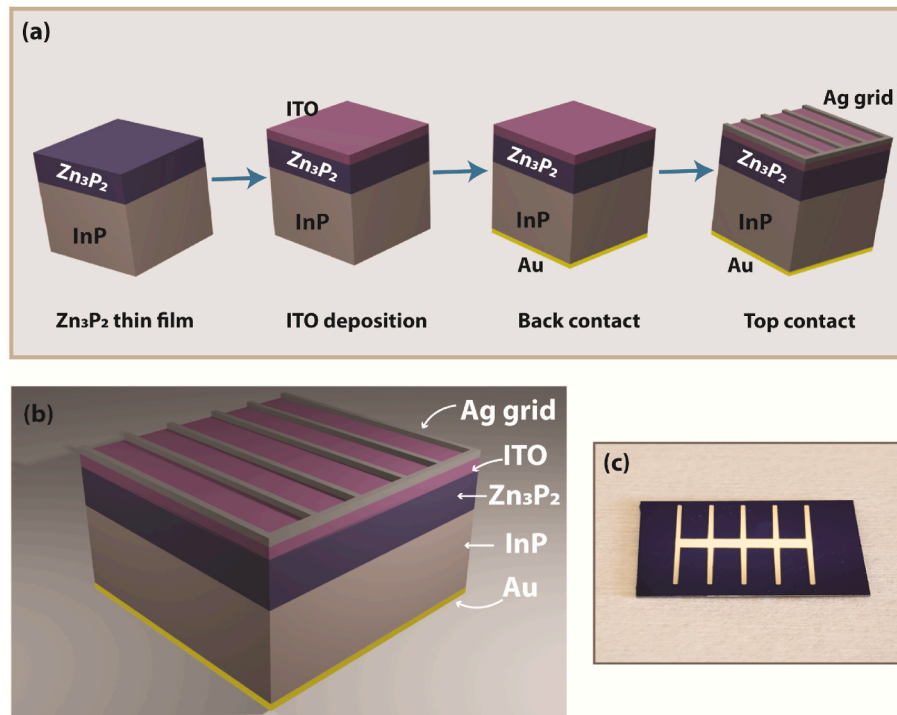


**Fig. 1.** (a) Schematic representation of the process employed for the fabrication of  $\text{Zn}_3\text{P}_2$  solar cell: ITO is deposited on the surface of the as-grown  $\text{Zn}_3\text{P}_2$  thin film with sputtering; followed by the deposition of Au as the back contact; and Ag is sputtered using a mask to form the top contact. (b) Schematic representation of the final device containing the Au back contact, InP substrate,  $\text{Zn}_3\text{P}_2$  thin film, sputtered ITO layer, and the Ag top contact. (c) Photograph of a fully fabricated cell.

## 2.2. Characterization methods

To first characterize the composition of the  $\text{Zn}_3\text{P}_2$  thin films, Rutherford backscattering spectrometry measurements were performed by EAG Laboratories. A nearly-normal-incident beam of 2.275 MeV alpha particles was used for the measurements, where the normal detector angle collected particles scattered by  $160^\circ$  and the grazing detector was set at  $104^\circ$ . The atomic concentration uncertainty is  $\pm 1\%$ , and an assumption of  $6.61 \times 10^{22}$  atoms/cm<sup>3</sup> in the  $\text{Zn}_3\text{P}_2$  layer and  $5.26 \times 10^{22}$  atoms/cm<sup>3</sup> in the InP substrate was used.

Following this, optical-pump terahertz-probe spectroscopy was performed to determine the optoelectronic properties of the thin films. These measurements were performed using a spectrometer with an ultrafast Ti:Sapphire amplifier (Newport Spectra Physics Spitfire Ace, 13 mJ, 1 kHz, 40 fs), which is described in detail in another study [23]. An optical pulse centered at 750 nm ( $E = 1.65$  eV) was used to photoexcite the sample with a pulse duration of 40 fs at fluences between 12 and 128  $\mu\text{J cm}^{-2}$ . The terahertz probe was generated by optical rectification in GaP crystal and was directed to the sample at an angle of incidence  $< 15^\circ$  by a silver-coated prism, which was positioned near the focus of the optical-pump terahertz-probe spectrometer at the sample position. The terahertz beam reflected from the sample was then collected via the same prism and detected by electro-optic sampling in a ZnTe crystal.

Finally, dark current-voltage (I-V) measurements were performed to assess the device performance using a Keithley 6487 voltage source and picoammeter to apply voltage and measure the current. The measurements were performed in the voltage range of  $\pm 1$  V. The light measurements were conducted using a solar simulator with continuous illumination, composed of a Halogen lamp (IR + VIS) and Xenon lamp (VIS + UV) with a temperature-controlled chuck. Measurements were performed according to the standard testing procedure (1-sun (1000 W/m<sup>2</sup>), AM 1.5 Global, 25 °C). For all the I-V measurements, one of the probes was placed on the Ag grid and the other on the rear contact. The

external quantum efficiency measurements were carried out using a Newport Oriel QuantX 300 tool. The basic gain was set to “1 M”; the wavelength spacing to 5 nm; the measurement range to 330–1000 nm; and the voltage bias to 0 V. The system calibration was checked using the reference Si solar cell of the system (red curve in Fig. 5e). The illumination-dependent I-V curves were measured using a Newport Oriel Sol2A tool. The I-V curve was measured with a measurement delay of 0.009 s, voltage steps of 2 mV, and measured going from -1 V to 1 V and from 1 V to -1 V. The intensity was checked with the system’s power calibration solar cell.

## 3. Results and discussion

### 3.1. Characterization of as-grown $\text{Zn}_3\text{P}_2$ thin films

We start by outlining the structural properties of the as-grown polycrystalline  $\text{Zn}_3\text{P}_2$  thin film. Fig. 2a shows the scanning electron microscopy (SEM) image of the thin film. The  $20^\circ$ -tilted SEM micrograph shows the cross-section and the top surface of the sample. The growth is granulated and columnar in nature with a coarse top surface. The thickness of the thin film was estimated to be  $\sim 0.7$   $\mu\text{m}$ . Previous studies have shown that grain boundaries in polycrystalline  $\text{Zn}_3\text{P}_2$  thin films are electrically passive with no detrimental effect on the photocurrent collection and the open-circuit voltage [24,25]. The composition of the thin film across the depth was analyzed using Rutherford backscattering spectrometry (RBS), as shown in Fig. 2b-c. In our previous work [26] we demonstrated the relation between the composition and the lattice constant of zinc phosphide. This work included cross-correlation between RBS, Energy dispersive X-ray spectroscopy, electron and X-Ray diffraction. The lattice of  $\text{Zn}_3\text{P}_2$  has demonstrated a high tolerance for compositional variations [26].  $\text{Zn}_3\text{P}_2$  can maintain its crystalline structure even at large off-stoichiometric compositions; the RBS measurements show a uniform composition of  $\sim 57\%$  zinc and

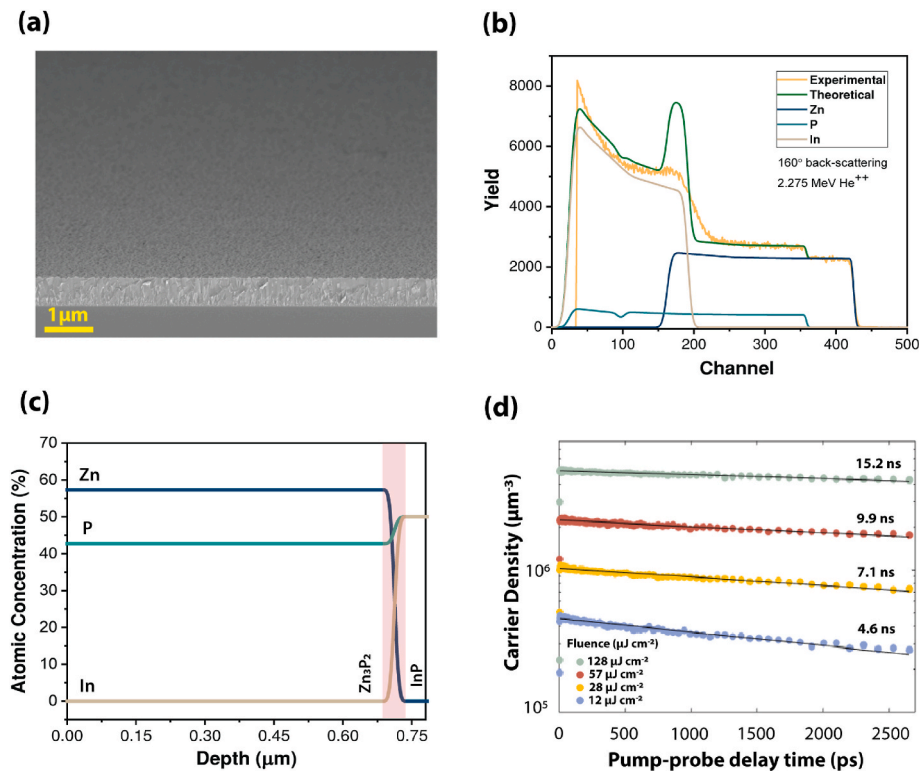


**Fig. 2.** (a) SEM image of the as-grown  $\text{Zn}_3\text{P}_2$  thin film on InP substrate. (b) Measured RBS spectrum in back-scattering ( $160^\circ$ ) and the fit of the spectrum (c) RBS measurements from  $\text{Zn}_3\text{P}_2$  thin film depicts a Zn/P ratio  $\approx 1.32$ . (d) The decay of photoinduced charge carrier density plotted as a function of pump-probe delay time measured by OPTP spectroscopy at different pump fluences, the lifetime for the corresponding fluence value is indicated on the graph.

~43% phosphorous. The thin film is slightly phosphorous rich, with a Zn:P ratio of 1.32 in comparison to 1.5 at stoichiometry (Zn:P = 60:40). Previous studies have shown that changes in the Zn:P ratio have no significant impact on the crystalline structure of the material, however, it can impact the functional properties of the material [11,27]. For more details on the impact of composition on optical and electrical properties, please refer to Refs. [26,28] respectively. More importantly, the carrier concentration in the material can significantly vary as excess phosphorous in the lattice acts as an acceptor-type impurity making the thin film p-type. To understand the temporal dynamics of the photoexcited carriers in the as-grown polycrystalline  $\text{Zn}_3\text{P}_2$  thin film, we used optical pump-terahertz probe (OPTP) spectroscopy. It is a versatile noncontact technique that is capable of measuring the photoconductivity and thereby the carrier mobilities, surface recombination velocities, carrier lifetimes, and doping levels of the material [29,30]. The measurements were conducted in reflection mode at room temperature and the sample was photoexcited with an optical pump with an FWHM of 1.2 mm, a centre wavelength of 750 nm, and with incident fluence values of 12, 28, 57, and 128  $\mu\text{J cm}^{-2}$ . The higher photon energy of the optical pump ( $E = 1.65 \text{ eV}$ ) compared to the bandgap of  $\text{Zn}_3\text{P}_2$  ( $E_g = 1.50 \text{ eV}$ ) provides above-bandgap photoexcitation, generating free electron-hole pairs in the  $\text{Zn}_3\text{P}_2$  thin film. While the photon energy of the pump is also above-bandgap for the InP substrate, the thickness of the  $\text{Zn}_3\text{P}_2$  film is greater than the absorption depth of photons with 750 nm wavelength. The majority of the optical pump photons are consequently absorbed within the  $\text{Zn}_3\text{P}_2$  film, so the InP substrate can be considered to be in equilibrium (i.e. not excited by the optical pump) with a negligible response on the measured THz response (see SI, Fig. S1). The above-bandgap photoexcitation, therefore, generates free electron-hole pairs predominately in the  $\text{Zn}_3\text{P}_2$  film, inducing a change in its dielectric function. This photoinduced change is measured by monitoring the change of the reflected electric field,  $\Delta E$ , of the terahertz probe,  $E$ . The ratio of the differential change in the reflected THz field compared to the response in equilibrium,  $\Delta E/E$ , is directly related to free carrier concentration and photoconductivity in the sample. Monitoring the change  $\Delta E/E$ , as a function of time after photoexcitation, therefore, provides information about the carrier recombination rates and carrier lifetimes of the thin film. Fig. 2d shows the variation in photoconductivity as a function of time after photoexcitation for different photoexcitation fluences. As the photoexcitation fluence was increased from 12 to 128  $\mu\text{J cm}^{-2}$  the extracted photoinduced carrier densities also increased from  $0.47 \times 10^{18} \text{ cm}^{-3}$  to  $5.01 \times 10^{18} \text{ cm}^{-3}$ . For all fluences, a sharp increase in the photoconductivity was observed within 10 ps after photoexcitation followed by a monoexponential decay. The characteristic decay times of the monoexponential fits of the carrier decay data are shown in the inset of Fig. 2c. A carrier lifetime of 4.6 ns was observed for 12  $\mu\text{J cm}^{-2}$ , whereas an increase in the carrier lifetime is observed with an increase in the laser fluence. The monoexponential decay indicates that monomolecular recombination (or trap-assisted recombination) is the

dominant recombination mechanism affecting the carrier lifetime. These values are consistent with the direct bandgap nature of the semiconductor.

### 3.2. Analysis of $\text{Zn}_3\text{P}_2/\text{InP}$ solar cells

Having investigated the material properties of the as-grown polycrystalline  $\text{Zn}_3\text{P}_2$  thin film, we now turn toward the demonstration of the photovoltaic device. The current density-voltage (J-V) curves of the device measured in dark and under simulated AM 1.5G 1-sun solar illumination are shown in Fig. 3a. The inset in Fig. 3a shows the photograph of the most representative device, which has an active area of  $0.467 \text{ cm}^2$ . The device is chosen accounting for the lower exposition of  $\text{Zn}_3\text{P}_2$  to atmosphere with respect to other samples which is expected to prevent performance degradation due to surface oxidation. Under simulated solar radiance, the open-circuit voltage ( $V_{oc}$ ) and short-circuit current ( $J_{sc}$ ) obtained from the device were 528.8 mV and  $13.7 \text{ mA/cm}^2$ , respectively. A fill-factor (FF) of 60.7% was measured, resulting in a power-conversion efficiency (PCE) of 4.4%. In contrast to the previous study on the  $\text{Mg}/\text{Zn}_3\text{P}_2$  Schottky junction solar cells [9], the  $V_{oc}$  shows a 7.5% improvement, whereas the  $J_{sc}$  is about 8% lower [9]. The series and shunt resistances are  $\sim 2.56 \Omega \text{ cm}^2$  and  $\sim 0.7 \text{ k}\Omega \text{ cm}^2$ , respectively. When comparing the J-V curves under illumination and in the dark, we observe that they do not superpose. There is a crossover behaviour at a voltage of around 537 mV [31]. One would need a higher voltage to achieve the same current density at the forward bias in the dark, compared to the curve obtained under illumination. Crossover is often associated with the presence of an electric barrier at the interface [32–36] as an illumination-dependent barrier height variation can lead to a crossover of dark and light J-V curves. Under illumination, this barrier height is reduced due to photodoping, thus resulting in a higher diode current [33,36]. The presence of a conduction band “spike” between ZnS and  $\text{Zn}_3\text{P}_2$  has shown similar crossover behaviour and it is known to hinder electron transport across the heterojunction interface in ZnS/ $\text{Zn}_3\text{P}_2$ -solar cells [37]. Another common reason for crossover behaviour is attributed to the high density of acceptor-like deep-level defects in the absorber near the interface region, which lead to a modification of the electric barrier. A strong potential drop associated with the large negative charge in the acceptor states leads to an electric barrier in the dark. Upon illumination, the acceptor states are filled with holes, resulting in a reduction in the acceptor charge and thereby decreasing the electric barrier [32,34,38,39]. Additionally, the illumination-dependent series resistance in solar cells is ascribed to photogating, which implies the excited carriers are captured in long-lived trap states, thereby increasing the conductivity [40,41]. This coincides with our OPTP measurements, which demonstrated that trap-assisted recombination was the dominant mechanism governing carrier transport in the  $\text{Zn}_3\text{P}_2$  thin films. However, it should be noted that the distortion in the J-V curve could be a combination of these

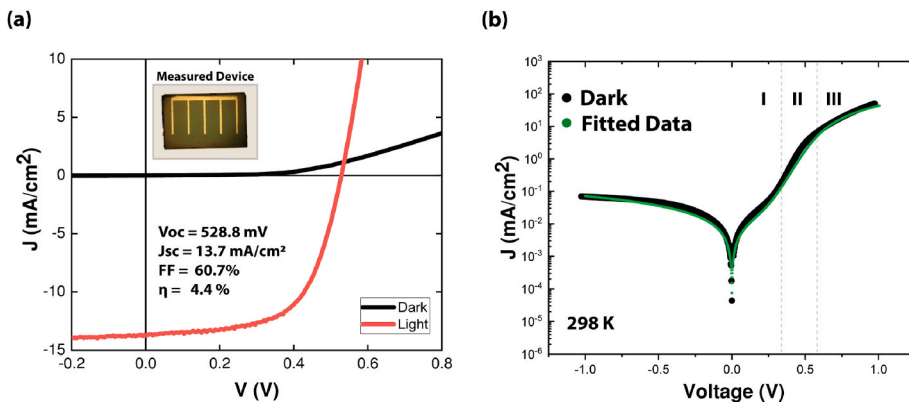


Fig. 3. (a) Representative J-V curves obtained in dark (denoted by black line) and under 1-sun illumination (denoted by red line), the inset shows the measured device that had an active area of  $0.467 \text{ cm}^2$ . (b) Dark J-V curve plotted in semi-logarithmic scale depicting the three distinct regions: region I corresponds to the voltage range  $< 0.25 \text{ V}$ ; region II corresponds to the voltage range between  $0.25 \text{ V}$  and  $0.53 \text{ V}$ ; region III corresponds to the voltage range  $> 0.53 \text{ V}$ . The numerical fitting of this data is depicted by the green dotted line.



effects [32,39].

To identify the dominant form of carrier recombination, one can look at the ideality factor of the solar cell, which is typically obtained from the Shockley diode equation. The Shockley diode equation is derived from drift-diffusion theory [42], and it is expressed as:

$$J_{\text{dark}} = J_0 \left[ \exp \left( \frac{V}{V_T n_{\text{id}}} \right) - 1 \right] \quad (1)$$

where  $J_{\text{dark}}$  is the dark current density,  $J_0$  is the saturation current,  $n_{\text{id}}$  is the ideality factor, and  $V_T = k_B T/q$  is the thermal voltage. The above equation does not take into account parasitic resistances. The ideality factor is described as a fitting parameter that determines how closely a diode behaviour matches the theory, ideally,  $n_{\text{id}} = 1$  for direct radiative recombination. However, when other types of bulk recombination dominate, the ideality factor is given by  $n_{\text{id}} = 2/\gamma$  where  $\gamma$  is reaction order. When  $\gamma = 1$ , it indicates first-order recombination (typically  $n_{\text{id}} = 2$  is associated with trap-assisted Shockley-Read-Hall (SRH) recombination) [43]. A  $\gamma$  value of 2 signifies bimolecular band-to-band recombination, whereas a  $\gamma$  value of 3 suggests trimolecular Auger recombination [44–46].

Fig. 3b depicts the dark J-V characteristic in a semi-logarithmic scale along with the fitted data. The dark J-V curve shows a rectifying behaviour and the curve can be divided into three distinct regions (as shown in Fig. 3b). At low voltages ( $<0.25$  V, region I), the selected device layout shows a low parasitical leakage current. In this low voltage region, the shunt resistance dominates the J-V characteristics. The presence of pinholes and micro-cracks in a device can serve as a shunt pathway [47]. A high shunt resistance is preferred to ensure a low leakage current, for the measured device the leakage current is low. A sharp increase in the current is observed at the intermediate voltage ( $0.25 < V < 0.53$ , region II) region. The sharp transition arises due to a diffusion-dominated current [48]. At high voltages ( $>0.53$ , region III), the dark J-V curve shows a shift to a less sharp current-voltage behaviour, consistent with a drift-dominated current flow expected at voltage values above the built-in potential. The drift-dominated current is limited by either the charge injection or the formation of space charge [49]. Additionally, the series resistance determines the J-V characteristics at the high voltage region, a steep slope in this region typically

indicates low series resistance [50]. It should be noted here that the ideality factor is determined from the regime below the built-in voltage, as solar cells operate below the built-in voltage. The ideality factor obtained from the numerical fit of the whole J-V curve was found to be  $\sim 2.1$ . Additionally, the ideality factor can be obtained from the slope of the semi-logarithmic dark J-V plot using Eq. (1), which is valid only in the exponential region. The ideality factor obtained on fitting the plot was 2.07. We also plot the ideality factor as a function of the applied bias (as shown in Fig. S2), where the ideality factor is obtained from the plateau value [51]. This method prevents erroneous fitting, as the exponential region is clearly distinguishable. The ideality factor values obtained from all methods are significantly larger than unity, indicating trap-assisted recombination plays a dominant role in the recombination process. This corroborates the monomolecular recombination behaviour obtained from the OOTP spectroscopy. Even though the device consists of an additional ITO layer and was exposed to additional fabrication processes, the predominant recombination mechanism remains the same.

Nonetheless, the interpretation of the ideality factor obtained from the dark J-V can be prone to errors. As the series and shunt resistance can influence the current dependence on voltage, it is difficult to attribute the variations in the estimated ideality factor as an influence of resistance (series and shunt) or recombination. Alternatively, we analyzed the  $V_{\text{oc}}$  as a function of illumination intensity. This method is also known as the Suns- $V_{\text{oc}}$  method and it is deemed more reliable as the measurement is performed in open-circuit condition, which eliminates the dependence on the parasitic series resistance [52–54]. Fig. 4a shows the systematic variation of the J-V curve of the thin film solar cell with respect to the illumination intensity of the solar simulator, where the incident nominal power is varied between 0 and  $1125 \text{ W/m}^2$  (0–1.125 suns). The  $V_{\text{oc}}$  obtained at 1.125 suns was  $\sim 0.5$  V for an aged device. The variation in the  $J_{\text{sc}}$ ,  $V_{\text{oc}}$ , and FF leads to a combined light-intensity dependence of the PCE. A sharp increase in the  $J_{\text{sc}}$  is observed, while the  $V_{\text{oc}}$  shows a gradual increase with the increase in light intensity. Moreover, there is a slight variation in the FF as a function of the light intensity. The solar cell parameters are extracted from the J-V curve and plotted individually as a function of the illumination intensity in Fig. 4b–d. The  $J_{\text{sc}}$  shows a monotonic increase with the increase in the

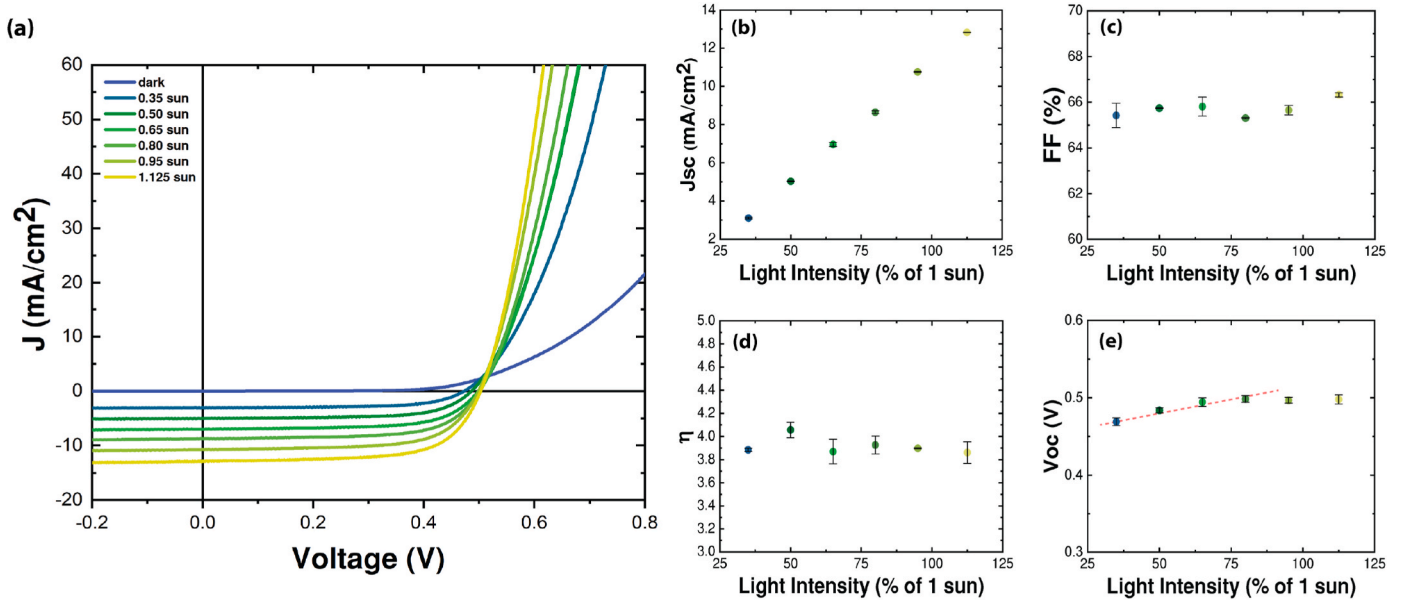
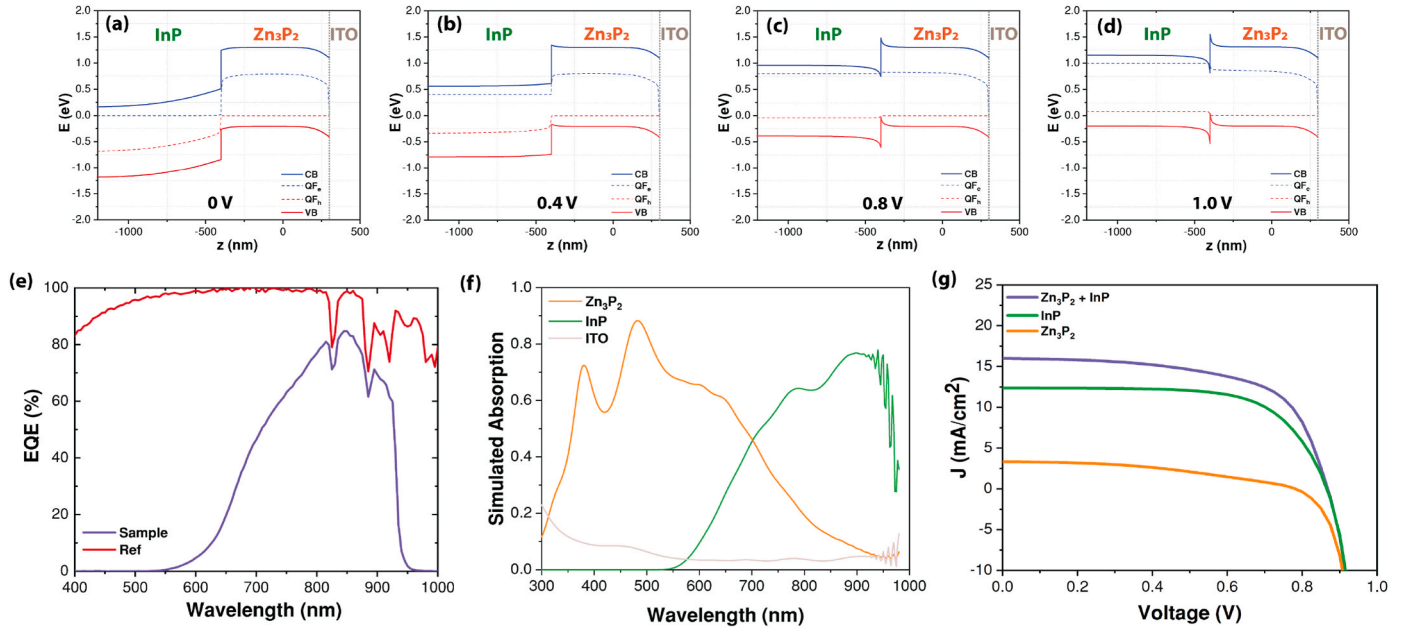


Fig. 4. (a) Light intensity dependence of J-V characteristics of the device, the measurements were performed at different illumination intensities ranging from 0 sun (dark) to 1.125 suns (which corresponds to  $1125 \text{ W/m}^2$ ). The different solar cell parameters are extracted from the light intensity dependent J-V curve and plotted as a function of the light intensity (b) short-circuit current density  $J_{\text{sc}}$ , (c) fill factor FF, (d) power conversion efficiency  $\eta$ , (e) open-circuit voltage  $V_{\text{oc}}$ , the red dashed line denotes the part of the plot used for extracting the ideality factor from the semi-logarithmic plot of light intensity against the  $V_{\text{oc}}$ .



**Fig. 5 (a–d).** Simulated band alignment between the  $\text{Zn}_3\text{P}_2$  layer and ITO at the front side, and the  $\text{Zn}_3\text{P}_2$  layer and InP at the back side, the blue solid line represents the conduction band (CB), the red solid line represents the valence band (VB), the blue dashed line depicts the quasi-fermi level for electrons ( $\text{QF}_e$ ), and the red line depicts the quasi-fermi level for holes ( $\text{QF}_h$ ), the simulation is done under different bias voltages (a) 0 V, (b) 0.4 V, (c) 0.8 V, and (d) 1 V. (e) The EQE obtained from the measured device (denoted with purple line) and the reference Si (denoted with red line). (f) Simulated absorption obtained from  $\text{Zn}_3\text{P}_2$  (denoted by the solid orange line), InP (denoted by the green solid line), and ITO (denoted by grey line) for the wavelength range of 300 nm–1000 nm. (g) Simulated I–V diagram obtained from  $\text{Zn}_3\text{P}_2$  generation (denoted by the solid orange line), from InP generation (denoted by the green solid line), and from the combined ( $\text{Zn}_3\text{P}_2$  and InP) generation (denoted by the solid purple line).

illumination intensity and shows no sign of saturation over the measured range of optical power, as shown in Fig. 4b. The FF obtained from  $P_{\text{max}}/(J_{\text{sc}}V_{\text{oc}})$  is plotted in Fig. 4c, where  $P_{\text{max}}$  denotes the output at the maximum power point. We observe a small variation in FF as a function of illumination intensity and the maximum FF (~66%) is reached at 1.125 suns. Additionally, the PCE is expressed as  $P_{\text{max}}/P_{\text{in}}$ , where  $P_{\text{in}}$  is the input power. Fig. 4d shows the variation in the PCE against the illumination intensity. We observe a PCE value of  $4 \pm 0.1\%$  throughout the range. It should be noted here that the J–V curve showing an efficiency of 4.4% (as shown in Fig. 3a) was obtained using a different setup, so a difference in the illumination input (power, spectrum, homogeneity) could lead to a slight discrepancy in the measured efficiencies. Additionally, the illumination power-dependent studies were done several weeks after fabrication, which could have resulted in the degradation of the device. Finally, the  $V_{\text{oc}}$  is plotted as a function of the light intensity, as shown in Fig. 4e. The  $V_{\text{oc}}$  increases steadily with the increase in the light intensity until 0.8 suns, with a slight fluctuation at higher illumination intensities. The slope of the semi-logarithmic plot of  $V_{\text{oc}}$  against the illumination intensity can be used for estimating the ideality factor, where the slope has the unit of  $kT/q$ . A change in the slope is observed at higher illumination intensities, which previous studies have attributed to the discrepancy in recombination mechanisms [53,55–59]. As mentioned previously, the ideality factor can be determined more reliably from the illumination intensity and the  $V_{\text{oc}}$  than the dark J–V curve. At the open-circuit and steady-state conditions, the integrated generation and recombination rates must be the same to ensure net zero current flow [54]. As the photogeneration is proportional to the illumination intensity, the ideality factor under illumination can be expressed as:

$$n_{\text{id},l} = \left( \frac{q}{k_B T} \frac{dV_{\text{oc}}}{d \ln(P_{\text{opt}})} \right) \quad (2)$$

where  $n_{\text{id},l}$  is the ideality factor under illumination, and  $P_{\text{opt}}$  is the illumination intensity. At open-circuit conditions, the ideality factor is

affected by the shunt resistance, however, the voltage drop over the series resistance is zero, which allows a more accurate description of the recombination mechanism. The ideality factor obtained on fitting the plot was found to be in the range of 1.02–1.3 (depending on the number of points considered for determining the slope), it should be noted that as the slope changes over higher illumination intensities, the last two points are neglected (when included, we obtain an ideality factor of 0.92). The results show a clear dominance of bimolecular recombination in presence of light. This shift from trap-assisted recombination in the dark ( $n_{\text{id}} > 1$ ) to band-to-band recombination under illumination ( $n_{\text{id},l} \approx 1$ ) has been previously reported [55,60–62]. Cowan et al. hypothesized that a higher density of charge carriers under illumination could lead to the shift from monomolecular to bimolecular recombination [56], as these recombination mechanisms have different density dependencies [51,63]. Alternatively, the difference in the ideality factor obtained from two methods could arise due to poor conductivities, which could give rise to large gradient in quasi-Fermi levels at  $V_{\text{oc}}$  [52].

Having assessed the recombination mechanism, we now turn to the contribution of  $\text{Zn}_3\text{P}_2$  and InP to the working device. Fig. 5a–d show the simulated band alignment between the  $\text{Zn}_3\text{P}_2$ , the ITO (on the front side) and an intrinsic InP substrate. We present the band alignment under an applied bias ranging between 0 and 1 V. The simulated band alignment indicates that the electrons drift in the direction from the  $\text{Zn}_3\text{P}_2$  to the InP and the holes in the opposite direction. This is in agreement with the polarity of the I–V curve given the direction of the applied bias. The collection of holes at the front of the device could be counterintuitive as ITO is traditionally used as an n-type contact and  $\text{Zn}_3\text{P}_2$  is a p-type semiconductor [20]. This would suggest that electron collection is facilitated at the  $\text{Zn}_3\text{P}_2$ -ITO interface. However, the junction with i-InP dominates the behaviour of the device and electrons are actually collected at the rear side of the device.

Fig. 5e presents the external quantum efficiency measurements (EQE) of the device as a function of wavelength. The EQE of solar cells corresponds to the conversion efficiency of the incident photons to collected electrons [64,65], which provides understanding of the charge

collection behaviour as a function of the energy of an incident photon. We observe a maximum EQE of 85% at  $\sim 847$  nm wavelength. A sharp rise in the EQE is observed at a wavelength of  $\sim 940$  nm, which corresponds to  $\sim 1.32$  eV. This value coincides with the absorption onset of InP (which has a bandgap of  $\sim 1.34$  eV), although there might be a slight contribution from the  $\text{Zn}_3\text{P}_2$  band tails [66–70]. The band gap of  $\text{Zn}_3\text{P}_2$  is widely reported to be 1.5 eV, and thus cannot account for the EQE contribution at energies below its bandgap. Still, a recent study by Stutz et al. demonstrated the presence of band tails that lead to band gap narrowing in  $\text{Zn}_3\text{P}_2$  (which gives rise to a high-intensity PL peak at 1.32 eV) [66]. This observation gives room to an alternative explanation, in which the  $\text{Zn}_3\text{P}_2$  already absorbs around the energy of the observed high-intensity PL peak. However, this would mean that the  $\text{Zn}_3\text{P}_2$  has an effective bandgap of around 1.32 eV instead, but at the same time does not explain why the EQE is 0% for wavelengths of 550 nm and lower, as  $\text{Zn}_3\text{P}_2$  demonstrates a high optical absorption coefficient in the visible spectral range [8]. To clarify the contribution of  $\text{Zn}_3\text{P}_2$  and InP to the measured EQE, we simulated the absorption of InP (10  $\mu\text{m}$  thick) and  $\text{Zn}_3\text{P}_2$  (700 nm thick), as shown in Fig. 5f. It can be seen that a significant part of the incident light is absorbed by the InP substrate. Additionally, the measured EQE and the simulated InP absorption show a large spectral overlap, while the simulated  $\text{Zn}_3\text{P}_2$  absorption spectrum cannot be recognized from the shape of the measured EQE curve. This suggests that the  $\text{Zn}_3\text{P}_2$  layer contributes significantly less to the measured EQE than the InP. To simulate the contribution of InP and  $\text{Zn}_3\text{P}_2$  to the overall current density, we selectively switched the charge carrier generation in the individual layers on and off, to obtain I–V curves for the different contributions, as shown in Fig. 5g. The orange line depicts the contribution from  $\text{Zn}_3\text{P}_2$ ; the green line depicts the contribution from InP. The simulation in Fig. 5g predicts that combining the two materials gives a higher current density (purple line), where the 700 nm of  $\text{Zn}_3\text{P}_2$  contributes only 3.3  $\text{mA}/\text{cm}^2$  to the overall current density. It is interesting to note that the simulated absorption predicts there could be a contribution of up to 18.2  $\text{mA}/\text{cm}^2$  from the 700 nm thick  $\text{Zn}_3\text{P}_2$ . In comparison, the InP contributes  $\sim 12.4$   $\text{mA}/\text{cm}^2$  and almost the same amount (13.0  $\text{mA}/\text{cm}^2$ ) is predicted from the simulated absorption. This indicates the internal quantum efficiency of InP is around 95%, whereas it is solely 18% for  $\text{Zn}_3\text{P}_2$ . The insufficient charge carrier extraction in the  $\text{Zn}_3\text{P}_2$  can be explained in the following way: we note that there is a slight downward bending in the CB of  $\text{Zn}_3\text{P}_2$  towards the ITO interface (as shown in Fig. 5a–d). This means that electrons that are generated within the first few hundreds of nanometers of the  $\text{Zn}_3\text{P}_2$  layer can get stuck and recombine instead of being collected at the back. The photo-generated carriers further away from the surface and in the vicinity of the InP and  $\text{Zn}_3\text{P}_2$  interface can be separated more efficiently. Thus, the reduced carrier collection from  $\text{Zn}_3\text{P}_2$  in comparison to InP is due to unfavorable energy alignment at the  $\text{Zn}_3\text{P}_2$ -ITO interface, which must be addressed in the future.

High energy photons are absorbed much closer to the surface, and hence are affected more strongly by the low extraction efficiency in the  $\text{Zn}_3\text{P}_2$ . This explains the EQE loss at shorter wavelengths. If the small  $\text{Zn}_3\text{P}_2$  contribution predicted by the simulations indeed also occurs experimentally, then it is spectrally overlapping with the InP contribution. Note that the comparison between experiment and simulation relies mainly on band alignment arguments, as the simulations assume fairly ideal bulk recombination parameters and no interface/surface recombination. Similar loss behaviour has been reported for  $\text{Zn}_3\text{P}_2/\text{ZnSe}$  heterojunction solar cells [19].

Here we propose an alternative device design to enhance the EQE and the overall efficiency of the device. Instead of ITO, a front contact with a larger work function could reduce the band bending at the front interface. Alternatively, to still utilize the transparency of the ITO, one could insert a dedicated hole-selective layer between the  $\text{Zn}_3\text{P}_2$  and ITO which would have an equivalent function. Passivation of the  $\text{Zn}_3\text{P}_2$  thin films has been shown to reduce the surface recombination velocity and could also be implemented [71] to reduce surface recombination effects.

To ensure efficient absorption in the  $\text{Zn}_3\text{P}_2$  layer, one should implement light trapping strategies with an antireflective coating, a back reflector and/or photonic design [72]. Realistically one could expect to increase the conversion efficiency to at least 10%. In the long term, a different substrate material has to be used along with the  $\text{Zn}_3\text{P}_2$  absorber layer, to make sure that light is solely absorbed in the dedicated  $\text{Zn}_3\text{P}_2$  layer.

#### 4. Conclusion

We demonstrated an efficiency of 4.4% for a solar cell consisting of polycrystalline  $\text{Zn}_3\text{P}_2$  thin film on an intrinsic InP substrate. The fabrication of the device only entails the deposition of a front ITO layer with metallic finger electrodes. We have identified some of the key limitations of the fabricated solar cell and the contribution of InP substrate to the photoconversion. These are poor carrier collection at the front electrode and a high series resistance. We believe the path toward high-efficiency  $\text{Zn}_3\text{P}_2$  solar cells entails a strategic device design, including the addition of an electron blocking layer at the front and improvement of light absorption in the  $\text{Zn}_3\text{P}_2$  by the implementation of antireflection and back-reflection layers as well as photonic structures. Ultimately, the InP substrate should be replaced by earth-abundant material like Si (for the nanostructure growth) or van der Waals substrates such as graphene [73].

#### CRedit authorship contribution statement

**Rajrupa Paul:** Writing – original draft, Investigation, Formal analysis, Conceptualization. **Stefan W. Tabernig:** Writing – review & editing, Software, Formal analysis, Data curation. **Joel René Saper:** Methodology, Formal analysis. **Julien Hurni:** Investigation. **Anja Tiede:** Investigation. **Xinyun Liu:** Investigation. **Djamshid A. Damry:** Investigation. **Vanessa Conti:** Investigation. **Mahdi Zamani:** Investigation. **Simon Escobar Steinvall:** Investigation. **Mirjana Dimitrievska:** Investigation. **Esther Alarcon-Lladó:** Writing – review & editing, Methodology, Investigation. **Valerio Piazza:** Writing – review & editing, Supervision, Investigation. **Jessica Boland:** Supervision, Formal analysis. **Franz-Josef Haug:** Supervision. **Albert Polman:** Writing – review & editing, Validation, Supervision, Methodology. **Anna Fontcuberta i Morral:** Writing – review & editing, Validation, Supervision, Resources, Project administration, Funding acquisition, Conceptualization.

#### Declaration of competing interest

The authors declare that they have no known competing financial interests or personal relationships that could have appeared to influence the work reported in this paper.

#### Data availability

Data will be made available on request.

#### Acknowledgements

The authors EPFL acknowledge the funding from SNF Consolidator Grant (BSCG10-157705). Authors also thank funding from Horizon Europe Pathfinder project SOLARUP. This work was supported by the Swiss State Secretariat for Education, Research and Innovation (SERI) under contract number 22.00153. V.P. gratefully acknowledges the funding from Piaget. M.D. thanks funding from H2020 through SMARTCELL project (project number: 101022257). The authors also acknowledge the CMI facilities of EPFL for their technical support. FJH and JH acknowledge support within the project ZIPPO of EPFL's interdisciplinary funding action eSeed. The authors from Manchester gratefully acknowledge support from EPSRC via project EP/S037438/1, UKRI via JLB's Future Leader Fellowship, MR/T022140/1 and from the



Leverhulme Trust via JLB's Philip Leverhulme Prize. They would also like to thank the University of Warwick for providing access to the Warwick Centre for Ultrafast Spectroscopy (WCUS) facility and Dr Michael Staniforth for conducting the initial THz spectroscopy measurements using the facility. J. L. B. also thanks Dr Christopher Beckler for fruitful discussions. The contributions of S.W. Tabernig and A. Polman are part of the research program of the Dutch Research Council (NWO).

## Appendix A. Supplementary data

Supplementary data to this article can be found online at <https://doi.org/10.1016/j.solmat.2023.112349>.

## References

- [1] Y. Cao, et al., Rotational design of charge carrier transport layers for optimal antimony trisulfide solar cells and its integration in tandem devices, *Sol. Energy Mater. Sol. Cell.* 206 (Mar. 2020) 110279, <https://doi.org/10.1016/j.solmat.2019.110279>.
- [2] J. Zhou, et al., Selective preferred orientation for high-performance antimony selenide thin-film solar cells via substrate surface modulation, *J. Alloys Compd.* 938 (Mar. 2023) 168593, <https://doi.org/10.1016/j.jallcom.2022.168593>.
- [3] Y. Cao, et al., Gradient bandgap modification for highly efficient carrier transport in antimony sulfide-selenide tandem solar cells, *Sol. Energy Mater. Sol. Cell.* 246 (Oct. 2022) 111926, <https://doi.org/10.1016/j.solmat.2022.111926>.
- [4] Y. Cao, et al., Epitaxial growth of Vertically aligned antimony selenide nanorod arrays for heterostructure based self-powered photodetector, *Adv. Opt. Mater.* 10 (19) (2022), 2200816, <https://doi.org/10.1002/adom.202200816>.
- [5] C. Wadia, A.P. Alivisatos, D.M. Kammen, Materials availability expands the opportunity for large-scale photovoltaics deployment, *Environ. Sci. Technol.* 43 (6) (Mar. 2009) 2072–2077, <https://doi.org/10.1021/es8019534>.
- [6] W. Shockley, H.J. Queisser, Detailed balance limit of efficiency of p-n junction solar cells, *J. Appl. Phys.* 32 (3) (Mar. 1961) 510–519, <https://doi.org/10.1063/1.1736034>.
- [7] E.A. Fagen, Optical properties of Zn3P2, *J. Appl. Phys.* 50 (10) (Oct. 1979) 6505–6515, <https://doi.org/10.1063/1.325746>.
- [8] M.Y. Swinkels, et al., Measuring the optical absorption of single nanowires, *Phys. Rev. Appl.* 14 (2) (Aug. 2020), 024045, <https://doi.org/10.1103/PhysRevApplied.14.024045>.
- [9] M. Bhushan, A. Catalano, Polycrystalline Zn3P2 Schottky barrier solar cells, *Appl. Phys. Lett.* 38 (1) (Jan. 1981) 39–41, <https://doi.org/10.1063/1.92124>.
- [10] G. Lombardi, F. Maia de Oliveira, M. Daldin Teodoro, A. Chiquito, Investigation of trapping levels in p-type Zn 3 P 2 nanowires using transport and optical properties, *Appl. Phys. Lett.* 112 (May 2018), 193103, <https://doi.org/10.1063/1.5026548>.
- [11] A. Catalano, R.B. Hall, Defect dominated conductivity in Zn3P2, *J. Phys. Chem. Solid.* 41 (6) (Jan. 1980) 635–640, [https://doi.org/10.1016/0022-3697\(80\)90015-3](https://doi.org/10.1016/0022-3697(80)90015-3).
- [12] N. Mirowska, J. Misiewicz, Defect-related transitions in Zn3P2 studied by means of photovoltaic effect spectroscopy, *Semicond. Sci. Technol.* 7 (11) (Nov. 1992) 1332–1336, <https://doi.org/10.1088/0268-1242/7/11/007>.
- [13] R. Katsube, H. Hayashi, A. Nagaoka, K. Yoshino, Y. Nose, Y. Shirai, Growth and characterization of indium-doped Zn3P2 bulk crystals, *Jpn. J. Appl. Phys.* 55 (Apr. 2016), <https://doi.org/10.7567/JJAP.55.041201>.
- [14] M. Bhushan, Schottky solar cells on thin polycrystalline Zn3P2 films, *Appl. Phys. Lett.* 40 (1) (Jan. 1982) 51–53, <https://doi.org/10.1063/1.92921>.
- [15] P.S. Nayar, A. Catalano, Zinc phosphide-zinc oxide heterojunction solar cells, *Appl. Phys. Lett.* 39 (1) (1981) 105–107, <https://doi.org/10.1063/1.92537>.
- [16] J.M. Pawlikowski, Preparation and characterization of close-spaced vapour transport thin films of ZnSe for heterojunction solar cells, *Thin Solid Films* 127 (1) (May 1985) 9–28, [https://doi.org/10.1016/0040-6090\(85\)90209-3](https://doi.org/10.1016/0040-6090(85)90209-3).
- [17] J.P. Bosco, S.B. Demers, G.M. Kimball, N.S. Lewis, H.A. Atwater, Band alignment of epitaxial ZnS/Zn3P2 heterojunctions, *J. Appl. Phys.* 112 (9) (2012), <https://doi.org/10.1063/1.4759280>.
- [18] K. Kakishita, K. Aihara, T. Suda, Zn3P2 photovoltaic film growth for Zn3P2/ZnSe solar cell, *Sol. Energy Mater. Sol. Cell.* 35 (C) (1994) 333–340, [https://doi.org/10.1016/0927-0248\(94\)90159-7](https://doi.org/10.1016/0927-0248(94)90159-7).
- [19] M. Bhushan, J.D. Meakin, Zn3P2 as an improved semiconductor for photovoltaic solar cells, *Mar* (1985). Accessed: Sep. 13, 2022. [Online]. Available: <https://ui.adsabs.harvard.edu/abs/1985delareptQ....B>.
- [20] T. Suda, M. Kobayashi, A. Kuroyanagi, S. Kurita, Zn3P2/ITO heterojunction solar cells, *Jpn. J. Appl. Phys.* 21 (S2) (Jan. 1982) 63, <https://doi.org/10.7567/JJAPS.21S2.63>.
- [21] O. Vazquez-Mena, et al., Performance enhancement of a graphene-zinc phosphide solar cell using the electric field-effect, *Nano Lett.* 14 (8) (Aug. 2014) 4280–4285, <https://doi.org/10.1021/nl500925n>.
- [22] M. Zamani, et al., The path towards 1  $\mu$ m monocrystalline Zn3P2 films on InP: substrate preparation, growth conditions and luminescence properties, *J. Phys. Energy* 3 (3) (May 2021), 034011, <https://doi.org/10.1088/2515-7655/abf723>.
- [23] M. Monti, et al., Efficient intraband hot carrier relaxation in the perovskite semiconductor Cs1-xRbxSnI3 mediated by strong electron-phonon coupling, *J. Phys. Chem. C* 122 (36) (Sep. 2018) 20669–20675, <https://doi.org/10.1021/acs.jpcc.8b07792>.
- [24] J.P. Bosco, G.M. Kimball, N.S. Lewis, H.A. Atwater, Pseudomorphic growth and strain relaxation of  $\alpha$ -Zn3P2 on GaAs(001) by molecular beam epitaxy, *J. Cryst. Growth* 363 (Jan. 2013) 205–210, <https://doi.org/10.1016/j.jcrysgro.2012.10.054>.
- [25] K.W. Mitchell, Status of new thin-film photovoltaic technologies, *Annu. Rev. Mater. Sci.* 12 (1) (1982) 401–413, <https://doi.org/10.1146/annurev.ms.12.080182.002153>.
- [26] E.Z. Stutz, et al., Stoichiometry modulates the optoelectronic functionality of zinc phosphide (Zn3-xP2+x), *Faraday Discuss* (Apr. 2022), <https://doi.org/10.1039/D2FD00055E>.
- [27] S.E. Steinvall, et al., Multiple morphologies and functionality of nanowires made from earth-abundant zinc phosphide, *Nanoscale Horiz* (Oct. 2019), <https://doi.org/10.1039/C9NH00398C>.
- [28] R. Paul, A. Fontcuberta I Morral, and V. Piazza, “Zn/P ratio and microstructure defines carrier density and electrical transport mechanism in earth-abundant Zn3-xP2+y thin films,” *Sol. Energy Mater. Sol. Cell.*...
- [29] H.J. Joyce, J.L. Boland, C.L. Davies, S.A. Baig, M.B. Johnston, A review of the electrical properties of semiconductor nanowires: insights gained from terahertz conductivity spectroscopy, *Semicond. Sci. Technol.* 31 (10) (Sep. 2016), 103003, <https://doi.org/10.1088/0268-1242/31/10/103003>.
- [30] J. Lloyd-Hughes, T.-I. Jeon, A review of the terahertz conductivity of bulk and nano-materials, *J. Infrared, Millim. Terahertz Waves* 33 (9) (Sep. 2012) 871–925, <https://doi.org/10.1007/s10762-012-9905-y>.
- [31] N.G. Tarr, D.L. Pulfrey, An investigation of dark current and photocurrent superposition in photovoltaic devices, *Solid State Electron.* 22 (3) (Mar. 1979) 265–270, [https://doi.org/10.1016/0038-1101\(79\)90032-7](https://doi.org/10.1016/0038-1101(79)90032-7).
- [32] C.-H. Chung, B. Bob, T.-B. Song, Y. Yang, Current-voltage characteristics of fully solution processed high performance CuIn(S,Se)2 solar cells: crossover and red kink, *Sol. Energy Mater. Sol. Cell.* 120 (Jan. 2014) 642–646, <https://doi.org/10.1016/j.solmat.2013.10.013>.
- [33] A.O. Pudov, J.R. Sites, M.A. Contreras, T. Nakada, H.-W. Schock, CIGS J-V distortion in the absence of blue photons, *Thin Solid Films* 480–481 (Jun. 2005) 273–278, <https://doi.org/10.1016/j.tsf.2004.11.099>.
- [34] M. Topić, F. Smole, J. Furlan, Examination of blocking current-voltage behaviour through defect chalcopyrite layer in ZnO/CdS/Cu(In,Ga)Se2/Mo solar cell, *Sol. Energy Mater. Sol. Cell.* 49 (1) (Dec. 1997) 311–317, [https://doi.org/10.1016/S0927-0248\(97\)00058-5](https://doi.org/10.1016/S0927-0248(97)00058-5).
- [35] A.O. Pudov, A. Kanevce, H.A. Al-Thani, J.R. Sites, F.S. Hasoon, Secondary barriers in CdS-CuIn1-xGaxSe2 solar cells, *J. Appl. Phys.* 97 (6) (Mar. 2005), 064901, <https://doi.org/10.1063/1.1850604>.
- [36] R. Scheer, H.-W. Schock, Thin film heterostructures, in: *Chalcogenide Photovoltaics*, John Wiley & Sons, Ltd, 2011, pp. 9–127, <https://doi.org/10.1002/9783527633708.ch2>.
- [37] J.P. Bosco, S.B. Demers, G.M. Kimball, N.S. Lewis, H.A. Atwater, Band alignment of epitaxial ZnS/Zn3P2 heterojunctions, *J. Appl. Phys.* 112 (9) (Nov. 2012), 093703, <https://doi.org/10.1063/1.4759280>.
- [38] A. Niemegeers, M. Burgelman, R. Herberholz, U. Rau, D. Hariskos, H.-W. Schock, Model for electronic transport in Cu(In,Ga)Se2 solar cells, *Prog. Photovoltaics Res. Appl.* 6 (6) (1998) 407–421, [https://doi.org/10.1002/\(SICI\)1099-159X\(199811/12\)6:6<407::AID-PIP230>3.0.CO;2-U](https://doi.org/10.1002/(SICI)1099-159X(199811/12)6:6<407::AID-PIP230>3.0.CO;2-U).
- [39] M. Burgelman, et al., Defects in Cu(In, Ga) Se2 semiconductors and their role in the device performance of thin-film solar cells, *Prog. Photovoltaics Res. Appl.* 5 (2) (1997) 121–130, [https://doi.org/10.1002/\(SICI\)1099-159X\(199703/04\)5:2<121::AID-PIP159>3.0.CO;2-4](https://doi.org/10.1002/(SICI)1099-159X(199703/04)5:2<121::AID-PIP159>3.0.CO;2-4).
- [40] M.M. Furchi, A. Pospischil, F. Libisch, J. Burgdörfer, T. Mueller, Photovoltaic effect in an electrically tunable van der Waals heterojunction, *Nano Lett.* 14 (8) (Aug. 2014) 4785–4791, <https://doi.org/10.1021/nl501962c>.
- [41] O. Lopez-Sanchez, D. Lembke, M. Kayci, A. Radenovic, A. Kis, Ultrasensitive photodetectors based on monolayer MoS2, *Nat. Nanotechnol.* 8 (7) (Jul. 2013), <https://doi.org/10.1038/nnano.2013.100>. Art. no. 7.
- [42] W. Shockley, The theory of p-n junctions in semiconductors and p-n junction transistors, *Bell System Technical Journal* 28 (3) (1949) 435–489, <https://doi.org/10.1002/j.1538-7305.1949.tb03645.x>.
- [43] C. Sah, R.N. Noyce, W. Shockley, Carrier generation and recombination in P-N junctions and P-N junction characteristics, *Proceedings of the IRE* 45 (9) (Sep. 1957) 1228–1243, <https://doi.org/10.1109/JRPROC.1957.278528>.
- [44] T. Kirchartz, B.E. Pieters, J. Kirkpatrick, U. Rau, J. Nelson, Recombination via tail states in polythiophene:fullerene solar cells, *Phys. Rev. B* 83 (11) (Mar. 2011), 115209, <https://doi.org/10.1103/PhysRevB.83.115209>.
- [45] O.J. Sandberg, A. Sundqvist, M. Nymän, R. Österbacka, Relating charge transport, contact properties, and recombination to open-circuit voltage in sandwich-type thin-film solar cells, *Phys. Rev. Appl.* 5 (Apr. 2016), 044005, <https://doi.org/10.1103/PhysRevApplied.5.044005>.
- [46] N.E. Courtier, Interpreting ideality factors for planar perovskite solar cells: ectypal diode theory for steady-state operation, *Phys. Rev. Appl.* 14 (2) (Aug. 2020), 024031, <https://doi.org/10.1103/PhysRevApplied.14.024031>.
- [47] O. Kunz, J. Wong, J. Janssens, J. Bauer, O. Breitenstein, A.G. Aberle, Shunting problems due to sub-micron pinholes in evaporated solid-phase crystallised poly-Si thin-film solar cells on glass, *Prog. Photovoltaics Res. Appl.* 17 (1) (2009) 35–46, <https://doi.org/10.1002/ppp.866>.
- [48] P. de Bruyn, A.H.P. van Rest, G.A.H. Wetzelaer, D.M. de Leeuw, P.W.M. Blom, Diffusion-limited current in organic metal-insulator-metal diodes, *Phys. Rev. Lett.* 111 (18) (Oct. 2013), 186801, <https://doi.org/10.1103/PhysRevLett.111.186801>.



- [49] G.-J.A.H. Wetzelaer, M. Scheepers, A.M. Sempere, C. Momblona, J. Ávila, H. J. Bolink, Trap-assisted non-radiative recombination in organic–inorganic perovskite solar cells, *Adv. Mater.* 27 (11) (2015) 1837–1841, <https://doi.org/10.1002/adma.201405372>.
- [50] J.D. Servaites, M.A. Ratner, T.J. Marks, Organic solar cells: a new look at traditional models, *Energy Environ. Sci.* 4 (11) (Oct. 2011) 4410–4422, <https://doi.org/10.1039/C1EE01663F>.
- [51] G.A.H. Wetzelaer, M. Kuik, H.T. Nicolai, P.W.M. Blom, Trap-assisted and Langevin-type recombination in organic light-emitting diodes, *Phys. Rev. B* 83 (16) (Apr. 2011), 165204, <https://doi.org/10.1103/PhysRevB.83.165204>.
- [52] W. Tress, et al., Interpretation and evolution of open-circuit voltage, recombination, ideality factor and subgap defect states during reversible light-soaking and irreversible degradation of perovskite solar cells, *Energy Environ. Sci.* 11 (1) (Jan. 2018) 151–165, <https://doi.org/10.1039/C7EE02415K>.
- [53] S. Ryu, N.Y. Ha, Y.H. Ahn, J.-Y. Park, S. Lee, Light intensity dependence of organic solar cell operation and dominance switching between Shockley–Read–Hall and bimolecular recombination losses, *Sci. Rep.* 11 (1) (Aug. 2021), <https://doi.org/10.1038/s41598-021-96222-w>. Art. no. 1.
- [54] T. Kirchartz, F. Deledalle, P.S. Tuladhar, J.R. Durrant, J. Nelson, On the differences between dark and light ideality factor in polymer:fullerene solar cells, *J. Phys. Chem. Lett.* 4 (14) (Jul. 2013) 2371–2376, <https://doi.org/10.1021/jz4012146>.
- [55] L.J.A. Koster, V.D. Mihailescu, R. Ramaker, P.W.M. Blom, Light intensity dependence of open-circuit voltage of polymer:fullerene solar cells, *Appl. Phys. Lett.* 86 (12) (Mar. 2005), 123509, <https://doi.org/10.1063/1.1889240>.
- [56] S.R. Cowan, W.L. Leong, N. Banerji, G. Dennler, A.J. Heeger, Identifying a threshold impurity level for organic solar cells: enhanced first-order recombination via well-defined PC84BM traps in organic bulk heterojunction solar cells, *Adv. Funct. Mater.* 21 (16) (2011) 3083–3092, <https://doi.org/10.1002/adfm.201100514>.
- [57] V.V. Brus, Light dependent open-circuit voltage of organic bulk heterojunction solar cells in the presence of surface recombination, *Org. Electron.* 29 (Feb. 2016) 1–6, <https://doi.org/10.1016/j.orgel.2015.11.025>.
- [58] R.A. Street, A. Krakaris, S.R. Cowan, Recombination through different types of localized states in organic solar cells, *Adv. Funct. Mater.* 22 (21) (2012) 4608–4619, <https://doi.org/10.1002/adfm.201200031>.
- [59] J. Vollbrecht, V.V. Brus, On the recombination order of surface recombination under open circuit conditions, *Org. Electron.* 86 (Nov. 2020), 105905, <https://doi.org/10.1016/j.orgel.2020.105905>.
- [60] S.R. Cowan, A. Roy, A.J. Heeger, Recombination in polymer–fullerene bulk heterojunction solar cells, *Phys. Rev. B* 82 (24) (Dec. 2010), 245207, <https://doi.org/10.1103/PhysRevB.82.245207>.
- [61] G.-J.A.H. Wetzelaer, M. Kuik, P.W.M. Blom, Identifying the nature of charge recombination in organic solar cells from charge-transfer state electroluminescence, *Adv. Energy Mater.* 2 (10) (2012) 1232–1237, <https://doi.org/10.1002/aenm.201200009>.
- [62] G.A.H. Wetzelaer, M. Kuik, M. Lenes, P.W.M. Blom, Origin of the dark-current ideality factor in polymer:fullerene bulk heterojunction solar cells, *Appl. Phys. Lett.* 99 (15) (Oct. 2011), 153506, <https://doi.org/10.1063/1.3651752>.
- [63] M. Kuik, H.T. Nicolai, M. Lenes, G.-J.A.H. Wetzelaer, M. Lu, P.W.M. Blom, Determination of the trap-assisted recombination strength in polymer light emitting diodes, *Appl. Phys. Lett.* 98 (9) (Feb. 2011), 093301, <https://doi.org/10.1063/1.3559911>.
- [64] S. Ravishankar, C. Aranda, Pablo P. Boix, J.A. Anta, J. Bisquert, G. Garcia-Belmonte, Effects of frequency dependence of the external quantum efficiency of perovskite solar cells, *J. Phys. Chem. Lett.* 9 (11) (Jun. 2018) 3099–3104, <https://doi.org/10.1021/acs.jpclett.8b01245>.
- [65] O. Almora, C.I. Cabrera, J. Garcia-Cerrillo, T. Kirchartz, U. Rau, C.J. Brabec, Quantifying the absorption onset in the quantum efficiency of emerging photovoltaic devices, *Adv. Energy Mater.* 11 (16) (2021), 2100022, <https://doi.org/10.1002/aenm.202100022>.
- [66] E.Z. Stutz, et al., Showcasing the optical properties of monocrystalline zinc phosphide thin films as an earth-abundant photovoltaic absorber, *Mater. Adv.* 3 (2) (Jan. 2022) 1295–1303, <https://doi.org/10.1039/D1MA00922B>.
- [67] M. Dimitrievska, et al., The advantage of nanowire configuration in band structure determination, *Adv. Funct. Mater.* 41/2021, *Adv. Funct. Mater.* 31 (41) (2021), 2170305, <https://doi.org/10.1002/adfm.202170305>.
- [68] P. Van Mieghem, Theory of band tails in heavily doped semiconductors, *Rev. Mod. Phys.* 64 (3) (Jul. 1992) 755–793, <https://doi.org/10.1103/RevModPhys.64.755>.
- [69] D. Shin, B. Saparov, D.B. Mitzi, Defect engineering in multinary earth-abundant chalcogenide photovoltaic materials, *Adv. Energy Mater.* 7 (11) (2017), <https://doi.org/10.1002/aenm.201602366>.
- [70] S.K. Wallace, D.B. Mitzi, A. Walsh, The steady rise of kesterite solar cells, *ACS Energy Lett.* 2 (4) (Apr. 2017) 776–779, <https://doi.org/10.1021/acsenenergylett.7b00131>.
- [71] G.M. Kimball, et al., Passivation of Zn3P2 substrates by aqueous chemical etching and air oxidation, *J. Appl. Phys.* 112 (10) (Nov. 2012), 106101, <https://doi.org/10.1063/1.4765030>.
- [72] P. Spinelli, M.A. Verschuuren, A. Polman, Broadband omnidirectional antireflection coating based on subwavelength surface Mie resonators, *Nat. Commun.* 3 (1) (Feb. 2012), <https://doi.org/10.1038/ncomms1691>. Art. no. 1.
- [73] R. Paul, et al., van der Waals epitaxy of earth-abundant Zn3P2 on graphene for photovoltaics, *Cryst. Growth Des.* 20 (6) (Jun. 2020) 3816–3825, <https://doi.org/10.1021/acs.cgd.0c00125>.